

# MIRD Pamphlet No. 26: Joint EANM/MIRD Guidelines for Quantitative $^{177}\text{Lu}$ SPECT Applied for Dosimetry of Radiopharmaceutical Therapy

Michael Ljungberg<sup>1</sup>, Anna Celler<sup>2</sup>, Mark W. Konijnenberg<sup>3</sup>, Keith F. Eckerman<sup>4</sup>, Yuni K. Dewaraja<sup>5</sup>, and Katarina Sjögreen-Gleisner<sup>1</sup>

In collaboration with the SNMMI MIRD Committee: Wesley E. Bolch, A. Bertrand Brill, Frederic Fahey, Darrell R. Fisher, Robert Hobbs, Roger W. Howell, Ruby F. Meredith, George Sgouros, and Pat Zanzonico, and the EANM Dosimetry Committee: Klaus Bacher, Carlo Chiesa, Glenn Flux, Michael Lassmann, Lidia Strigari, and Stephan Walrand.

<sup>1</sup>Department of Medical Radiation Physics, Lund University, Lund, Sweden; <sup>2</sup>Radiology Department, Medical Imaging Research Group, University of British Columbia, Vancouver, Canada; <sup>3</sup>Department of Nuclear Medicine, Erasmus University Medical Center, Rotterdam, Holland; <sup>4</sup>Easterly Scientific, Knoxville, Tennessee; and <sup>5</sup>Department of Radiology, University of Michigan Medical School, Ann Arbor, Michigan

The accuracy of absorbed dose calculations in personalized internal radionuclide therapy is directly related to the accuracy of the activity (or activity concentration) estimates obtained at each of the imaging time points. MIRD Pamphlet no. 23 presented a general overview of methods that are required for quantitative SPECT imaging. The present document is next in a series of isotope-specific guidelines and recommendations that follow the general information that was provided in MIRD 23. This paper focuses on  $^{177}\text{Lu}$  (lutetium) and its application in radiopharmaceutical therapy.

**Key Words:** image processing; oncology; endocrine; radiobiology/dosimetry; radionuclide therapy; SPECT/CT; guideline; lutetium; quantitative SPECT

**J Nucl Med 2016; 57:151–162**  
DOI: 10.2967/jnumed.115.159012

The radionuclide  $^{177}\text{Lu}$  (lutetium) has been proven useful in several targeted radionuclide therapies because of its favorable decay characteristics and the possibility of reliable labeling of biomolecules used for tumor targeting. Initially,  $^{177}\text{Lu}$  was used in a colloidal form for interstitial injections for sterilization of peritumoral lymph nodes (1). A second important clinical application of  $^{177}\text{Lu}$  has been for peptide receptor radionuclide therapy (PRRT) with  $^{177}\text{Lu}$ -DOTATATE and other structurally related peptides. The PRRT use in treatment of neuroendocrine tumors (NETs) is motivated by the fact that the carrier peptide, octreotate, shows high-affinity binding to somatostatin receptors, which are overexpressed on the cell surface of many NETs (2–6). Furthermore,  $^{177}\text{Lu}$  has

been used in radioimmunotherapy clinical trials to label different kinds of monoclonal antibodies (7–15).

There is a growing body of evidence that radionuclide therapy should follow patient-specific planning protocols, similar to those that are being routinely used in external-beam radiation therapy. Recent literature reviews show correlations between absorbed dose and tumor response as well as normal-tissue toxicity (16). Such correlations indicate that treatments should be based on personalized dosimetry, aiming to deliver therapeutically effective absorbed doses to tumors, while keeping doses to organs at risk below the threshold levels for deterministic adverse effects. In clinical PRRT studies, the primary adverse effects have been mainly renal and hematologic toxicities (2,6).

Although several studies have reported estimates of absorbed doses (4,7–9,12) for  $^{177}\text{Lu}$ -DOTATATE PRRT and  $^{177}\text{Lu}$  radioimmunotherapy, most of these estimates have been based on planar imaging and conjugate-view activity quantification. Planar imaging, however, is known to have inherent limitations regarding the accuracy of activity quantification (17). As a result, an increasing number of clinical dosimetry protocols currently include  $^{177}\text{Lu}$  SPECT/CT imaging studies (15,17–19) because of their superior accuracy. Comparisons of renal dose estimates in  $^{177}\text{Lu}$ -DOTATATE PRRT based on planar imaging and SPECT/CT, for example, have been reported (17,20) and are summarized in Cremonesi et al. (21).

This document presents a set of guidelines outlining data acquisition protocols and image reconstruction techniques that are recommended for quantitative  $^{177}\text{Lu}$  SPECT imaging. The guidelines are based on a review of the literature and are illustrated by the results of Monte Carlo simulations and phantom experiments and by the examples of patient  $^{177}\text{Lu}$  SPECT studies in which renal doses due to PRRT were estimated.

## DECAY OF $^{177}\text{Lu}$

$^{177}\text{Lu}$  decays by  $\beta^-$  emissions to  $^{177}\text{Hf}$  (hafnium) with a half-life of 6.65 d (22). The maximum kinetic energy of  $^{177}\text{Lu}$   $\beta^-$  particles is 498.3 keV (23), and the mean kinetic energy of all emitted  $\beta^-$  particles is approximately 134 keV. Additionally, 6 groups of  $\gamma$ -photons and associated internal-conversion electrons

Received May 7, 2015; revision accepted Oct. 1, 2015.  
For correspondence or reprints contact: Michael Ljungberg, Department of Medical Radiation Physics, Clinical Science, Lund, Lund University, SE-221 85 Lund, Sweden.  
E-mail: michael.ljungberg@med.lu.se  
Published online Oct. 15, 2015.  
COPYRIGHT © 2016 by the Society of Nuclear Medicine and Molecular Imaging, Inc.

are emitted. When all emitted electrons ( $\beta^-$ , conversion, and Auger electrons) are considered, the mean kinetic energy rises to 147 keV. Two of these  $\gamma$ -photons, with the energies of 112.9 (6.17%) and 208.4 keV (10.36%), have been successfully used in  $^{177}\text{Lu}$  imaging studies. Table 1 summarizes information about  $^{177}\text{Lu}$   $\gamma$ -photon energies and intensities based on previous studies (22–28). Moreover, bremsstrahlung radiation generated by interactions of  $\beta^-$ -particles with tissue may be observed. Bremsstrahlung yield, however, is low (0.012 bremsstrahlung photons per decay for a  $^{177}\text{Lu}$  source in water [C.F. Uribe, P.L. Esquinas, H. Piwowarska-Bilska, et al., unpublished data, 2013]), and most (~85%) of these photons have energies below 50 keV. Nevertheless, some of them can contribute to the background recorded in the low-energy part of the spectrum.

## DATA ACQUISITION

The choice of collimator in imaging studies is a trade-off between the need for high system sensitivity to achieve good signal-to-noise ratio and spatial resolution in images and the need to minimize septal penetration of high-energy photons. If the collimator septa are not thick enough, a large number of photons that penetrate or scatter in the collimator septa will be detected, resulting in decreased image contrast, degradation of spatial resolution, and increased image artifacts, leading to difficulties in accurate activity distribution quantification.

Table 2 illustrates these issues by comparing system sensitivities (cps/MBq) for imaging studies performed using the 113- and 208-keV photopeaks. The data in this table represent sensitivities per camera detector calculated using Monte Carlo simulations (29) and 20% energy windows centered at 113 and 208 keV. Four types of collimators of the Infinia family of collimators (GE Healthcare) and 2 NaI(Tl) crystal thicknesses were investigated. The modeled source was a 10-cm-diameter  $^{177}\text{Lu}$  Petrilike disk placed in air at 10 cm from the collimator surface. Additionally, for each case the fractions of the detected counts due to collimator scatter and septal penetration are shown in parentheses.

Although in general the system sensitivity is higher for low-energy general-purpose (LEGP) or low-energy high-resolution (LEHR) collimators than for medium-energy (ME) or high-energy (HE) collimators, ME collimators are preferable for  $^{177}\text{Lu}$  imaging because of their lower septal penetration of the high-energy pho-

tons emitted by  $^{177}\text{Lu}$ . On the other hand, although HE collimators have slightly better sensitivity than ME collimators for 208-keV photons, they have inferior spatial resolution due to their wider collimator holes.

For 208-keV photons, a thicker 5/8" scintillation crystal provides higher sensitivity than the standard 3/8" crystal, which decreases the statistical noise in the image for any given acquisition time and activity. For example, for a 5/8"-thick crystal thickness, the number of photons detected in a 20% energy window centered at 208 keV increases by about 35% as compared with that for a 3/8" crystal. However, the sensitivity for the 113-keV window is higher for the 3/8" crystal than the 5/8" crystal as a result of contribution from 208-keV photons that have been backscattered in the material behind the crystal. The energy of 208-keV photons scattered at 180° is 114.6 keV. For a thinner crystal, the probability of a 208-keV photon passing through the crystal increases, thereby increasing the contribution from backscatter. Also the high-energy photons from the  $^{177}\text{Lu}$  decay can back scatter and contribute to the image counts.

If a ME collimator is used, the data should be collected in a 15%–20% energy window centered on the 208-keV photopeak. If the number of count collected in the 208-keV window is considered insufficient, a second energy window centered on the 113-keV photopeak can be used. It is recommended that the 2 datasets be acquired into separate projection files and reconstructed into 2 separate images (each image individually compensated for attenuation and scatter using appropriate attenuation maps [AMs]). Only when the quality of the images obtained from the lower-energy projections is deemed acceptable (i.e., the images obtained from the 113-keV window have an image appearance similar to those from the 208-keV window) should they be summed for further analysis.

If using a low-energy collimator (LEHR or LEGP), a single 20% energy window centered on the lower 113-keV photopeak is preferable, as in this case the contribution from septal penetration severely deteriorates the image acquired in the 208-keV photopeak window (30). However, in the 113-keV energy window a significant portion of the acquired counts will originate from the high-energy photons that have scattered in the patient and the collimator. This effect can be seen in the data presented in Table 2. These scattered photons considerably increase the background in

**TABLE 1**  
Compilation of Energies and Intensities of  $\gamma$ -Ray Emissions (%) Per Nuclear Decay of  $^{177}\text{Lu}$

keV	Reference					
	Schötzig et al. (24)	Deepa et al. (23)*	Kossert et al. (25)	Eckerman et al. (26)	Kondev (27)	Kondev et al. (22) and NuDat2.6 (28)
71.6	0.1734	0.1844	0.1720	0.154	0.1726	0.172
112.9	6.17	6.44	6.22	6.40	6.20	6.17†
136.7	0.0464	0.0563	0.0492	0.0480	0.0470	0.0469
208.4	10.36	10.36	10.55	11.0	10.38	10.36†
249.7	0.1987	0.2053	0.2023	0.212	0.2012	0.2008
321.3	0.2074	0.2559	0.2111	0.219	0.216	0.210

\*Intensities were calculated on the basis of Deepa et al. (23) in which normalization assuming 208-keV photopeak intensity of 100 was used.

†Values are recommended for use in this work.

**TABLE 2**

Simulated (National Electrical Manufacturers Association) System Sensitivity Per Camera Detector (cps/MBq)<sub>FOV</sub> for  $^{177}\text{Lu}$  Photopeaks and Several Imaging Conditions

Crystal	Collimator*	113-keV window		208-keV window	
		15%	20%	15%	20%
3/8"	HE	6.8 (3.0%)	7.5 (3.1%)	7.0 (6.8%)	7.2 (6.9%)
3/8"	ME	5.8 (3.3%)	6.3 (3.5%)	6.0 (7.8%)	6.1 (8.0%)
3/8"	LEGP	16.1 (31.8%)	18.6 (35.4%)	71.5 (84.7%)	74.6 (84.9%)
3/8"	LEHR	12.0 (43.5%)	14.3 (47.9%)	70.3 (90.4%)	73.2 (90.5%)
5/8"	HE	6.7 (2.9%)	7.3 (2.9%)	9.5 (6.9%)	9.8 (7.0%)
5/8"	ME	5.7 (3.2%)	6.2 (3.3%)	8.1 (7.8%)	8.3 (7.9%)
5/8"	LEGP	14.1 (22.7%)	16.0 (26.0%)	95.1 (84.4%)	98.6 (84.5%)
5/8"	LEHR	9.9 (32.3%)	11.4 (36.1%)	92.9 (90.1%)	96.6 (90.3%)

\*GE Infinia camera.

Fractions of detected counts that are due to collimator scatter and septal penetration are shown in parentheses. Some contribution to 113-keV window comes from events from 208-keV photons Compton-scattered in crystal followed by an escape. This contribution increases with decreasing crystal thickness.

the 113-keV photopeak energy window. Thus, accurate scatter correction becomes essential.

These effects are visualized in Figures 1–3. The data presented in these figures were generated using Monte Carlo simulations (29) of a SPECT system with a 5/8" NaI(Tl) crystal and energy resolution with a full width at half maximum of 9.5% at 140 keV. The patient was simulated using an XCAT digital male phantom (31), with activity distribution based on a typical patient imaging study performed 24 h after an injection of 7.4 GBq  $^{177}\text{Lu}$ -DOTATATE.

Figure 1 compares energy spectra of the detected photons for LEGP and ME collimators. Although both spectra correspond to the same source activity, their shapes and counting rates are different. Both spectra have high scatter background in the lower-energy region. However, because of collimator septal penetration, in the spectrum acquired with the LEGP collimator the 208-keV photopeak has a significantly higher counting rate than the 113-keV photopeak, despite similar decay intensities of these 2 transitions

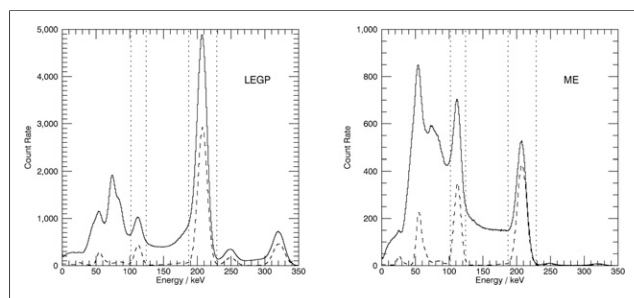


**FIGURE 1.** Simulated energy spectra of 7.4 GBq of  $^{177}\text{Lu}$  distributed in XCAT phantom imaged with LEGP and ME collimators (GE Infinia). Solid lines represent total spectra, whereas dashed lines show spectra of primary photons that pass unscattered through phantom and collimator. Dotted lines indicate 20% energy windows centered at 113- and 208-keV photopeaks. Note difference (due to photon scatter and collimator septal penetration) in both shape of spectra and in their counting rates.

(Table 1). Not only is the counting rate of the 208-keV photopeak about 4 times higher than that of the 113-keV photopeak, but also some lower-abundance higher-energy photopeaks, such as 249.7 and 321.3 keV, are clearly visible. In the spectrum acquired with the ME collimator (with its thicker septa and therefore less septal penetration) the measured intensities better reflect the true emission rates.

To further illustrate the negative effect of septal penetration on image quality, Figure 2 displays 4 projections simulated for these 2 collimators (LEGP and ME) and for the 2 energy windows (113

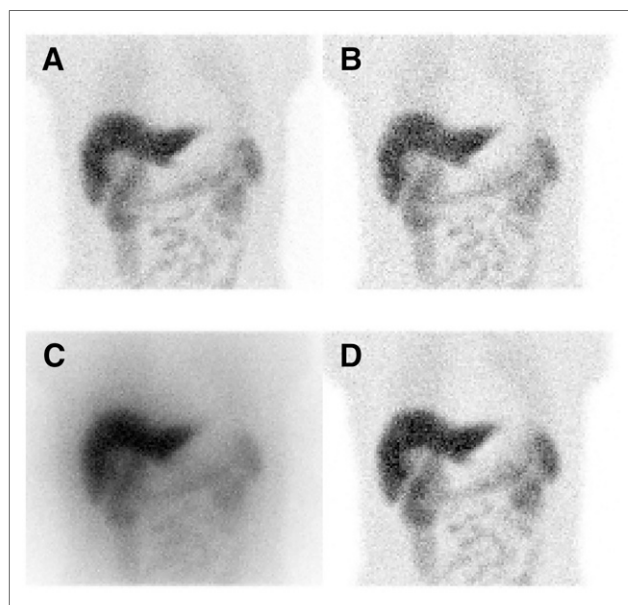


**FIGURE 2.** Simulated projections of  $^{177}\text{Lu}$  distributed in XCAT phantom showing difference in image quality obtained with LEGP and ME collimators (GE Infinia) and 2 energy windows (113 and 208 keV). (A) LEGP and 113-keV window. (B) ME and 113-keV window. (C) LEGP and 208-keV window. (D) ME and 208-keV window.

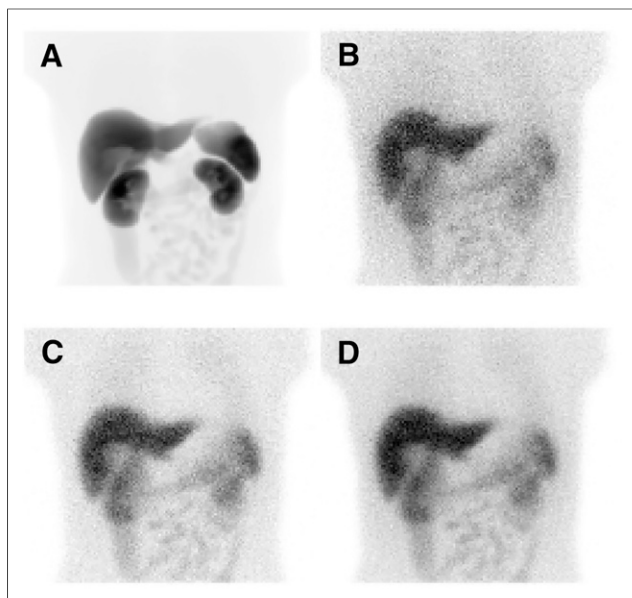


**FIGURE 3.** Simulated projection images of XCAT phantom corresponding to typical  $^{177}\text{Lu}$ -DOTATATE imaging study at 24 h after injection. (A) Image simulated by assuming scintillation camera with perfect spatial resolution and no attenuation and scatter in phantom. Because no interactions occur, this image is representative for both 113- and 208-keV energy window. (B) Image simulated with ME collimator (GE Infinia), photon attenuation and scatter included and with a realistic noise level for 20% energy window centered on 113 keV. (C) Image shows same as for B but for 20% energy window centered on 208 keV. (D) Image showing sum of 2 images shown in B and C.

and 208 keV). To better visualize the penetration effect, the simulation did not include scatter and attenuation in the phantom. These data suggest that the ME collimator provides the best image quality for both energy windows and is therefore more suitable for use in imaging.

In addition to the penetration effect, the contributions from photons scattered in the patient also influence both the image quality and the ability to quantify activity. To illustrate this additional unwanted scatter contribution, Figure 3 shows simulated anterior projection images (32) obtained using the ME collimator. Figure 3A represents an idealized imaging situation when the spatial resolution is perfect (i.e., the simulation does not include blurring due to detector spatial resolution and collimator response), photons pass unscattered from the site of decay to the detector and deposit their full energy in the crystal. The 208-keV energy window was used for this image. Figures 3B and 3C represent realistic images that include effects of limited collimator resolution (collimator blurring) and scatter and attenuation in the object for energy windows centered at 113 and 208 keV, both with window widths of 20%. Figure 3B shows that the image acquired in the 113-keV energy window had a higher background of scattered photons and decreased image contrast as compared with Figure 3D, which corresponds to the 208-keV window. Figure 3D shows the sum of the data obtained in these 2 energy windows.

Additionally, on the basis of these simulations, the scatter-to-total ratios for the whole projection, that is, the fractions of detected photons that have been scattered in the phantom to the total number of detected events, were estimated. Simulations were

performed for 2 crystal thicknesses, 2 photopeak energy windows settings, 4 collimators, and acquisitions using separately each of the  $^{177}\text{Lu}$  photopeaks and a combination of both. The results are presented in Table 3.

Examination of the values summarized in Table 3 shows that, when the 208-keV energy window was used, the scatter-to-total ratio in most cases was in the range of 0.17–0.27, with values slightly lower for higher crystal thicknesses. This ratio was much higher, however, and equaled about 0.47–0.60 for the 113-keV energy window. This increase was partly caused by the increased detection of self-scattered 113-keV photons but mostly was due to a large contribution of downscattered 208-keV photons into this window. The scatter-to-total ratio slightly improved with a 15% energy window, and depended only weakly on the crystal thickness. Thus, when a 113-keV window is used it is important to use a reliable scatter correction method to compensate for this large scatter fraction.

For  $^{177}\text{Lu}$  SPECT, acquisition in  $128 \times 128$  projection matrices is advisable if the counting rates allow for it (33). Autocontour orbits should be used to get the best possible image resolution. The use of autocontouring also makes acquisition preparation easier and thereby improves the overall efficiency of the patient study. Clinical  $^{177}\text{Lu}$  SPECT imaging studies using 60–120 projection angles have been reported (17,19,20).

## DATA PROCESSING

### Filtering

The need for low-pass filtering of the projection data may arise if the count levels resulting in high image noise are observed. To avoid bias in the activity determination, the user should verify that the total counts in the data (in the projections or in the reconstructed image) remain unchanged after filtering.

If a collimator–detector response (CDR) compensation is applied during the reconstruction, this compensation changes the noise texture in the image, which may make pre-/postreconstruction low-pass filtering unnecessary. However, the decision about

**TABLE 3**  
Ratios of Scattered Photons to Total Number of Photons Detected Within Energy Window (15% or 20%)

Crystal	Collimator*	113-keV window		208-keV window	
		15%	20%	15%	20%
3/8"	HE	0.60	0.55	0.27	0.22
3/8"	ME	0.60	0.55	0.27	0.22
3/8"	LEGP	0.53	0.49	0.21	0.18
3/8"	LEHR	0.49	0.47	0.20	0.17
5/8"	HE	0.60	0.56	0.27	0.22
5/8"	ME	0.60	0.56	0.26	0.22
5/8"	LEGP	0.55	0.52	0.20	0.17
5/8"	LEHR	0.53	0.49	0.20	0.17

\*GE Infinia camera.

Results of this simulation with XCAT phantom are presented as a function of 2 crystal thicknesses and 4 collimators.

filtering should be based on the specific objectives of the study (34,35).

### Dead Time

Although in principle, in radionuclide therapy imaging the count losses related to dead-time (DT) effects can be substantial, in  $^{177}\text{Lu}$  imaging, the DT effects are actually rather small (even for high activities) because of the low yield of  $\gamma$ -photons emitted in the decay of  $^{177}\text{Lu}$  and the very small bremsstrahlung contribution. For  $^{177}\text{Lu}$ -DOTATATE patients, it is mainly scans obtained shortly after the therapeutic injection that can be affected by DT losses, especially if the urinary bladder is included in the field of view (FOV). However, even if the DT effects are modest, care must be taken to estimate them, especially for scans obtained shortly after the therapeutic injection.

The count losses due to DT estimated from the entire spectrum can be significantly lower (by a factor of 2 or more (36)) than when only count losses in the photopeak window are considered. This is because the pile-up effects change the distribution of counts in the spectrum. When a new scintillation event occurs before the light from previous events has decayed, the recorded energy will be higher than expected. As a result, some counts are shifted from the photopeak region but still are recorded in the high-energy part of the spectrum (37). The spatial localization of the event can also be affected, because the  $x,y$ -coordinates are determined from the centroid of the scintillation light emission. There is also a possibility for scattered photons to pile up in the photopeak window, especially for lower-energy window locations, such as the 113-keV window, for which the separation in energy between scattered and primary photons is smaller. Therefore, because images are reconstructed from the photopeak counts only, the determination of the DT correction factor should be parameterized on the basis of the counts recorded in the whole spectrum, but only the count losses in the photopeak window should be described.

One way of addressing the DT problem is to perform a series of phantom experiments with gradually decaying activity, using the same acquisition protocol and scatter correction as used for patient studies. Analysis of count losses in these phantom images can be used to establish DT correction factors as a function of counting rate for any particular camera system. In this type of DT measurements, it is recommended to use a phantom that as closely as possible models an average patient in both size and activity distribution.

As an alternative to the phantom-based estimation of DT losses, the DT correction factor could be estimated from planar imaging performed in conjunction with the patient SPECT scan. In this method, a small marker source is placed at the edge of the FOV of the camera, and planar scans over the SPECT FOV with and without the patient (38) are obtained. The ratio of counts from these 2 scans (obtained from data acquired in the photopeak window and corrected for scatter) in a region of interest (ROI) around the marker provides the DT correction factor to be used for patient studies. The drawback of this method is the additional acquisition time required for these planar scans (with and without the patient). It has been suggested (39) that the DT correction factor can be determined using a 5- to 10-min planar patient scan acquired in close connection to the tomographic acquisition. The DT correction factor can also be determined from multiple projection views (40).

As the dead time will very likely affect only scans obtained shortly after injection (the first time point in the time-activity curve), it may have little effect on the overall absorbed dose calculation because of the relatively small contribution of this first time point to the cumulated activity.

### Iterative Reconstruction

Accurate quantification requires compensation for image-degrading factors. Iterative reconstruction methods, such as the maximum likelihood expectation maximization algorithm (41) and the ordered-subsets expectation maximization (OSEM) algorithm (42), provide the ability to compensate for these effects in a unified manner and are thus typically used and recommended (33).

Iterative methods require a certain number of updates before reaching an acceptable image quality. This implies that a criterion to determine the number of iterations is used. MIRD pamphlet 23 (33) defines the convergence as when the 90% recovery has been reached, which states this is a level of high reconstruction accuracy. A general rule of thumb is that more complex reconstruction problems (in which more corrections are included in the algorithm) require a larger number of iterations to reach convergence. It is important to investigate this dependency and optimize reconstruction parameters using data from phantom studies and simulations but also sample patient data with representative activity distributions and counting statistics.

The number of iterations required for convergence for a given number of subsets also depends on the organ size. Figure 4 illustrates this effect using an example of the reconstruction of a  $^{177}\text{Lu}$ -DOTATATE patient SPECT/CT scan. The total activity in volumes of interest (VOIs) drawn around the kidneys and a tumor is plotted as a function of the number of OSEM updates (number of subsets multiplied by number of iterations). Because the true activity is not known in this case, the curves have been normalized to the highest activity value obtained for each VOI. For this particular case, the volume of the tumor was similar to that of the kidneys. It can be seen that a smaller number of iterations was required for convergence for the kidneys than for the tumor. The slope of the tumor curve diminishes earlier than that for the kidneys, but after 200 updates when the kidneys show convergence the tumor still shows an upward trend to the maximum value. If following the 90% of maximum activity as being a measure for recovery, the tumor reaches this level at 20 updates whereas the right kidney needs 40 updates. For 95%, however, all VOIs reach this level at 60 OSEM updates.

In general, because image noise tends to be amplified as the number of iterations increases, when interpreting data derived from SPECT images (e.g., using dose-volume histograms), it is important to remember that high variations in voxel counts may be caused by the reconstruction process and may not necessarily be related to a heterogeneous biologic uptake of the radiopharmaceutical.

### PHOTON ATTENUATION

The most important factor altering the number of photons that impinge on the  $\gamma$ -camera detector is photon attenuation. The thickness of tissue-equivalent material that reduces the fluence of 208-keV photons to half is only about 5 cm. Because this attenuation depends on the density of the medium, an accurate attenuation correction (AC) must be based on patient-specific AMs (33).

How AMs used for AC are determined depends on the camera system, but if possible, it is recommended that a CT study is used for this purpose, preferably acquired using a SPECT/CT camera.

The accuracy of image quantitation critically depends on the accuracy of attenuation coefficients that are input into AC. Therefore, when CT-based AM is used, the accurate translation of CT images from Hounsfield numbers to attenuation coefficients corresponding to the energies of the  $^{177}\text{Lu}$  photopeaks must be performed.

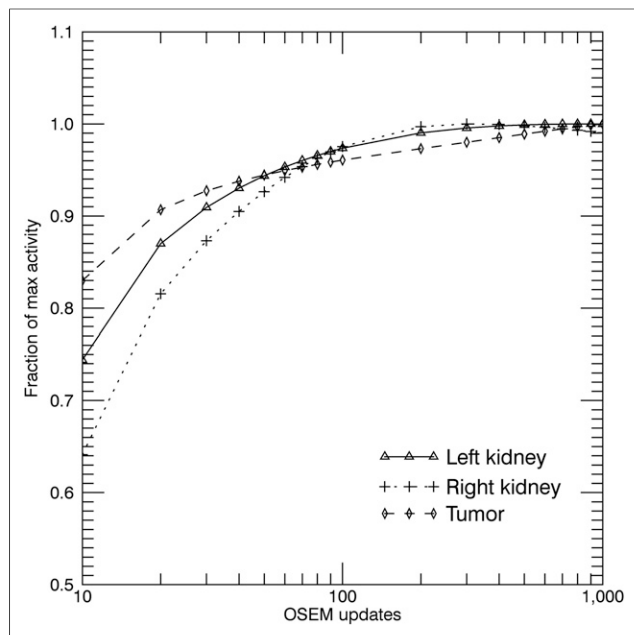


**FIGURE 4.** Total activity in VOIs normalized to highest activity obtained for particular VOI for different number of OSEM updates. Reconstructions included compensations for attenuation, scatter, and collimator response. Analysis was performed using VOIs delineated in consecutive slices over kidneys and tumor in patient study.

Additionally, because CT and SPECT data use different matrices and voxel sizes, the CT images must be properly registered to align with SPECT images and interpolated to match SPECT matrix sizes. Finally, AMs should be smoothed so that their resolution matches the SPECT resolution to reduce potential edge effects at boundaries, in regions displaying large attenuation gradients (such as those at soft-tissue/air, lung/soft-tissue, and soft-tissue/bone interfaces). As a result, because the creation of AMs from CT images is a complex procedure, requiring proprietary information about both CT and SPECT systems, it is therefore recommended that AMs reconstructed using manufacturer's software are used.

If both 208- and 113-keV photopeaks are used for imaging, 2 separate AMs must be generated and images reconstructed.

Given the importance of AC, a quality control protocol must be developed to ensure that the AM reflects correct attenuation coefficient values for the major classes of tissues (lungs, tissue, and bone). Additionally, the accuracy of the alignment of the AM and SPECT image must be checked because CT and SPECT scans are always obtained sequentially and the patient may move between or during scans (43).

### COMPTON SCATTER

Each photopeak energy window will also contain events from scattered photons (34), as shown in Table 3. For  $^{177}\text{Lu}$  studies, this will include both self-scattered photopeak photons (i.e., scattered photons that initially had the energy equal to the photopeak energy of the considered energy window) and downscattered photons from high-energy transitions.

The use of scatter correction is especially important for 113-keV-based imaging because of the large contribution from downscattered high-energy photons in this window.

A practical correction technique is the triple-energy-window (TEW) method (44). Two additional windows, set on both sides of the photopeak, allow the user to account not only for the self-scatter but also for downscattered high-energy photons. The compensation method can be described by

$$SE_{pw} = \left( \frac{C_{lw}}{W_{lw}} + \frac{C_{uw}}{W_{uw}} \right) \times \frac{W_{pw}}{2}, \quad \text{Eq. 1}$$

where  $C_{lw}$  and  $C_{uw}$  are pixel counts in lower and upper windows, respectively, and  $W_{lw}$ ,  $W_{uw}$ , and  $W_{pw}$  are the respective widths of lower, upper, and photopeak windows, respectively. The window widths must be carefully selected, because too-narrow windows will result in a high noise level in the scatter image (45). Usually energy windows are selected to have the width (in percentage) equal to one half of the width (46) or the same width (30,47) as the photopeak window, unless another photopeak prevents it. Such a situation occurs, for example, if a scatter energy window is to be set below the 113-keV photopeak, where lead x-ray photons may interfere.

Subtraction pixel by-pixel of estimated scatter projections from the photopeak projection image results in noise amplification or even negative counts (48). Better results are obtained when the scatter estimate is incorporated into the projector step in the iterative reconstruction algorithm. Additionally, because a ME collimator the scatter energy window set above the 208-keV photopeak usually contains relatively few counts, this second scatter window can be ignored (45,46).

For most  $^{177}\text{Lu}$  studies, applying the TEW scatter correction will result in relatively good quantitative accuracy of activity distributions. This is because a window-based correction method compensates not only for the self-scattered photons, but also for the background beneath the photopeak that is created by scattered high-energy photons. Thus, reasonably accurate quantitative images can be reconstructed from studies performed with low-energy collimators and 113-keV photopeak or ME collimators and 208 keV only or ME collimators and both photopeaks.

However, the scattered photons recorded in the lower energy window originate from locations different from those in the photopeak window. Moreover, many of the scattered high-energy photons recorded in the scatter window may have scattered several times before being detected. For these reasons, the TEW correction does not accurately reproduce the distribution of scattered photons in the photopeak window, particularly in regions with nonuniform density distributions. This effect is illustrated in Figure 5, which compares projection images A and C of the true distributions of scatter in 208- and 113-keV energy windows, respectively, with the corresponding TEW-estimated scatter images B and D. The true scatter images are sharper than those obtained with the TEW method. However, these differences are usually small, especially in the abdomen region illustrated in this figure; they are mostly smaller than 10%.

Scatter compensation can also be performed using a direct modeling of scatter in the projector step of the reconstruction method. For instance, the effective scatter source estimation (ESSE) method, developed by Frey et al. (49,50), uses precalculated kernels obtained from Monte Carlo simulations to estimate self-scatter in the photopeak window, whereas the analytic photon distribution interpolative (APDI) method (51,52) uses the Klein-Nishina cross-section for Compton scattering to analytically calculate scatter distribution in projections.

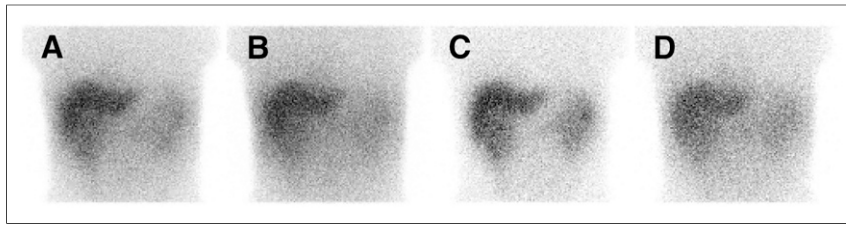


**FIGURE 5.** Row of images showing comparison of true scatter distributions (A and C) from  $^{177}\text{Lu}$  photons and those estimated by TEW scatter compensation method (B and D) for 113-keV energy window (A and B) and for 208-keV energy window (C and D) (20%). Scatter distributions were simulated using XCAT phantom, and settings for scatter windows for TEW method were [lw = 88–102, uw = 125–153] keV for 113-keV photopeak and [lw = 153–187] keV for 208-keV photopeak. Upper TEW window for 208-keV photopeak was set to zero because of few scatter events and contribution from 249-keV photon from  $^{177}\text{Lu}$  decay. Collimator parameters represent GE Infinia camera.

For situations when the density distribution is nonuniform, improved image quality and quantitative accuracy can be obtained if scatter models, such as the ESSE or APDI, are used. Both the ESSE and the APDI methods have been successfully applied to  $^{177}\text{Lu}$  phantoms studies (30,45).

#### COLLIMATOR–DETECTOR RESPONSE (CDR)

The collimator–detector blurring, which affects the spatial resolution of the image, varies with the source-to-collimator distance (33). For LEHR and ME collimators, typical spatial resolutions of the system measured at 10 cm are about 8 and 10 mm, respectively. Additionally, septal penetration and scatter in the collimator can further reduce image contrast and spatial resolution (Table 2).

Reconstruction algorithms, which include geometric CDR compensation, modify the distribution of counts in the image but do not

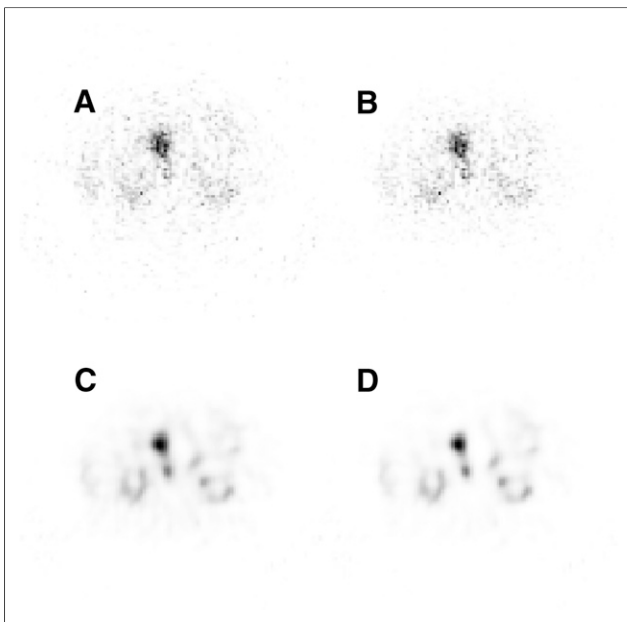


**FIGURE 6.** OSEM reconstructed images (80 OSEM updates) from  $^{177}\text{Lu}$ -DOTATATE patient study measured at 24 h after injection. (A) No corrections. (B) AC only. (C) Attenuation and collimator compensation corrections. (D) Attenuation, ESSE scatter, and collimator response compensation. No postfiltering has been applied.

change their total number. Therefore, they do not affect the quantification of the total activity in the field of view. CDR compensation not only improves spatial resolution, but also changes the noise texture so that the image appears smoother. The improvement depends in a complex way on the signal-to-background ratio, noise levels in the data, camera orbit, and the number of iterations. When quantifying the total activity in an organ or tumor, a reconstruction with CDR compensation may be beneficial because it decreases the resolution-induced spill-out of counts from hot regions.

However, CDR compensation may create Gibbslike artifacts (ringing artifacts) in the vicinity of sharp boundaries

(53) and thereby change the distribution of counts within a VOI. When the distribution of absorbed doses for individual voxel locations is calculated within a VOI for further analysis using dose–volume histograms, one should be aware of the fact that CDR correction may result in creation of false dose–volume information (35).

Figure 6 illustrates 4 types of reconstructed images of the kidney region. The image in Figure 6D corresponds to the one used clinically in the Lund protocol described in detail in the “Patient Examples” section. Images (A–C) are displayed to show the impact of different compensation methods on image quality.

#### ACTIVITY QUANTIFICATION

##### Camera Calibration

Reconstructed images represent the 3-dimensional distributions of voxel values obtained by measuring photons emitted from the imaged object. To convert voxel values to activity, the camera system must be carefully calibrated using a radioactive source with a well-determined  $^{177}\text{Lu}$  activity (34). Furthermore, it is important to ensure that the activity meter (dose calibrator) used to measure the activity of  $^{177}\text{Lu}$  calibration source is correctly calibrated with a well-known (i.e., independently calibrated)  $^{177}\text{Lu}$  activity, preferably one that is traceable to a standard laboratory. Care must also be taken that the same source geometry (same vials and the same volume of activity-containing solution) used in these measurements will be used for clinical studies, because the dose calibrator measurement is source-geometry dependent.

Different approaches can be used to determine the camera calibration factor, depending on how accurately attenuation and scatter corrections are implemented (33). If corrections are accurate (i.e., the reconstructed image truthfully represents the distribution of emitted photons), calibration can be performed by simply acquiring a planar image of a small pointlike source placed in air. The calibration factor for the camera (cps/MBq)<sub>FOV</sub> is then determined from the total counts in a ROI surrounding the source image, divided by the acquisition time and activity. However, potential contribution to the ROI from the high-energy  $^{177}\text{Lu}$  scattered photons may need to be accounted for (using an appropriate scatter correction method, e.g., TEW) (54).

Alternatively, a large water cylinder containing a well-calibrated source of  $^{177}\text{Lu}$  can be scanned. The same acquisition protocol and reconstruction method (with corrections) as was used in patient studies must be used. Again, the calibration factor is then

determined by dividing the total counts in the reconstructed image of the phantom by the scan time and activity. These 2 methods, namely, planar acquisition of a small source and tomographic scanning of an extended source, should ideally result in the same calibration factor (54).

### Quantification of Activity in VOIs

In radionuclide therapies with  $^{177}\text{Lu}$ -DOTATATE, because kidneys are considered to be the main organ at risk, the renal absorbed dose is of interest. When using a SPECT/CT system with high-resolution CT, the kidney VOI can be drawn using anatomic images from the CT part of the study. However, because of activity spill-out resulting from partial-volume effects (33), the kidney activity determined from the volumes obtained from CT will be underestimated. Partial-volume effects also blur the boundaries of regions, making determination of their exact location difficult, thus imposing uncertainties on activity measurements. The CDR incorporated into the reconstruction algorithm reduces the spill-out to some extent, making it easier to determine the activity content of a VOI. However, it is important to be aware of the artifacts that may be introduced by CDR in the form of rims with increased activity (Gibbs artifacts).

Several software-based methods have been proposed to correct for partial-volume effects (53), but in most cases their implementation in routine clinical practice is limited by their complexity. Probably the simplest and most commonly used method is to apply experimentally determined recovery coefficients, RCs, as described in a study by Dewaraja et al. (33). For patient studies, the activity  $A_{\text{VOI}}$  contained in a VOI is then determined as a product of 3 parameters, according to

$$A_{\text{VOI}} = \text{CPS}_{\text{VOI}} \times \frac{1}{\text{RC}_{\text{OBJ}}} \times \frac{1}{\left(\frac{\text{CPS}}{\text{MBq}}\right)_{\text{FOV}}}, \quad \text{Eq. 2}$$

where the first parameter,  $\text{CPS}_{\text{VOI}}$ , is the counting rate measured in an image VOI; the second parameter,  $\text{RC}_{\text{OBJ}}$ , is the recovery coefficient for an object, which best represents the VOI dimensions in the patient image; and the third parameter is the system sensitivity (cps/MBq). An example of a recovery coefficient curve for  $^{177}\text{Lu}$  determined using a series of spheres with different sizes placed in a phantom has been described by Ilan et al. (55). The values of RCs not only depend on the object size and shape, but also are strongly influenced by data acquisition protocol and image reconstruction method, so RCs need to be determined for each camera/collimator and data acquisition/reconstruction protocol.

### Time-Activity Curves

Quantitative information about temporal changes in activity distribution is required for determination of time-activity curves and time-integrated activity concentrations (33). If it is not possible to acquire SPECT scans at multiple time points (e.g., due to time constraints), a hybrid planar/SPECT approach is sometimes used (33). Here, the time-activity curves are determined from a time series of planar whole-body scans that have been corrected for attenuation, scatter, and overlapping activity contribution. At one time point, an additional quantitative SPECT study is also performed. Each time-activity curve is then rescaled by the ratio of activities determined for the organ/region corresponding to this time-activity curve from the SPECT image and the whole-body (i.e., planar) study.

## PHANTOM IMAGING STUDIES

In patient studies, the evaluation of quantitative accuracy of reconstructed images is extremely difficult (if not impossible) because in this case true values of activity are not known and usually cannot be independently determined. However, such evaluation can be done using phantom experiments. Therefore, although it is generally acknowledged that even the most sophisticated phantoms are not able to reproduce the complexity of activity and tissue distributions encountered in patients, phantom experiments are often used to determine the accuracy of imaging methods. Additionally, to compare and combine image-derived absorbed dose values obtained at different centers (possibly using different camera systems, imaging protocols, and reconstruction algorithms), phantom studies are recommended for cross-calibration.

Several issues related to quantitation of  $^{177}\text{Lu}$  imaging studies have been investigated using phantom experiments. These include comparison of different approaches to determine camera normalization factors (54); investigation of dead-time effects and appropriate correction methods (39,46); and comparison of the accuracy of image quantitation, which can be achieved when using 113- or 208-keV photopeaks for the camera equipped with LEHR and ME collimators (30,46).

In particular, to evaluate the accuracy of image quantitation, experiments with spheric and cylindrical objects filled with  $^{177}\text{Lu}$  activity placed in air and in water without and with background activity have been performed. Image reconstructions used OSEM algorithms with CDR compensation available on commercial cameras (46) or reconstruction methods developed in-house (30). All reconstructions used CT-based AC, whereas for scatter correction the dual-energy window method (DEW) (30,46), TEW (45,56), ESSE (45), and APDI (30) methods were investigated. Table 4 summarizes the results of these studies.

## CLINICAL APPLICATIONS OF $^{177}\text{Lu}$

In early animal experiments, it was shown that after injection the  $^{177}\text{Lu}$  salts transform to hydroxide and form colloids, which are cleared by phagocytosis to regional lymph nodes (1). Animal biodistribution studies have demonstrated that approximately 60% of soluble  $^{177}\text{Lu}$  salts circulating in the bloodstream will concentrate in the skeleton, resulting in high absorbed doses (57).

Presently,  $^{177}\text{Lu}$  is used in PRRT for treatment of NETs, in some cases parallel to or in conjunction with  $^{90}\text{Y}$ . In most centers DOTATATE or DOTATOC is used, and all patients are injected with the same 7.4-GBq activity repeated in 4–6 therapy cycles. Clinical PRRT trials show favorable outcomes in terms of progression-free survival and overall objective response rate (2,6). However, improved treatment outcomes could be expected if the injected activities would be based on personalized dosimetry calculations and image-based therapy plans.

Personalized dosimetry in PRRT aims to determine the maximum administered activity that will result in an absorbed dose that will be well tolerated by the patient with little or no side effects of renal and hematologic toxicities (2,6). Kidney irradiation is usually prolonged due to tubular reabsorption of radiolabeled peptides, and therefore coinjection of amino acids is often performed for renal protection. When  $^{177}\text{Lu}$ -DOTATATE is used, permanent renal toxicity has been considerably less frequent compared with that for  $^{90}\text{Y}$ -DOTATOC (3,6).

The limits for absorbed dose to the kidneys have been set at either 23 Gy (19,58) or 27 Gy (17,59). The use of the biologically effective dose allows for comparisons of therapies using a different

**TABLE 4**  
Recent Phantom Experiments Evaluating Accuracy of Quantification of <sup>177</sup>Lu Activity

Reference	Photopeak energy	Phantom	Reconstruction	Segmentation	Accuracy
Beauregard et al. (46)	208 keV	Three 175-mL cylinders in cold water	OSEM, CDR, AC, DEW scatter correction	40% fixed threshold	<15% for cylinders, <9.5% for total phantom activity
Shcherbinin et al. (30)	113 keV	70 mL cylinder placed in air and cold water	OSEM, CDR, AC, APDI scatter correction	CT volume augmented by 4 voxels in each direction	1%–2% for cylinder VOIs, <11%–18% for total phantom activity
Uribe et al. (56)	208 keV	0.5- to 113-mL spheres in air, cold and hot water	OSEM, CDR, AC, TEW scatter correction	Fixed threshold 0.1% for air, 1% for water, iterative adaptive dual thresholding (66) for hot water	<3% for spheres, >1 mL in air, <13% for spheres, >1 mL in water, <3% for 113-mL sphere in hot water
		8.5- to 34-mL bottles in air and cold water	OSEM, CDR, AC, TEW scatter correction		<5% in air, <13% in water
		Four 34-mL cylinders in thorax phantom (nonuniform cold environment)	OSEM, CDR, AC, APDI scatter correction		<5%
		34- to 148-mL cylinders in air and between cold water bags	OSEM, CDR, AC, TEW scatter correction		<7%
de Nijs et al. (45)	208 keV	27-mL spheric insert in National Electrical Manufacturers Association phantom	OSEM, CDR, AC		
			TEW (15%)		11%
			TEW (20%)		12%
			ESSE		7%

number of cycles and other radionuclides such as <sup>90</sup>Y. On the basis of these studies, new kidney dose limits of 28 and 40 Gy (depending on the presence of additional risk factors) have been proposed (4). A study from Uppsala (19) showed that only 20% of patients reached the lower 23-Gy threshold after 3 cycles of 7.4 GBq and that 50% of the patients were treated using more than 4 cycles. These results clearly indicate that a standard protocol of 7.4 GBq administered activity in 4 cycles may lead to an under-treatment for large groups of patients, as the maximum therapeutic response rate (i.e., the combination of percentage of patients showing partial and complete response after therapy) by <sup>177</sup>Lu is 35% (2,6). Personalized dosimetry may allow for better tailoring of the administered <sup>177</sup>Lu activity or the number of treatment cycles to the needs of each individual patient.

#### PATIENT EXAMPLES

Individualized dosimetry-based treatment planning in <sup>177</sup>Lu-DOTATATE PRRT has been reported separately by both Uppsala

Academic Hospital and Lund University Hospitals (17,19,20). Currently, a clinical study is ongoing in collaboration between Lund and Sahlgrenska University Hospital, Gothenburg, Sweden. Details of these clinical studies provided in the following sections exemplify 2 different approaches to clinical quantitative <sup>177</sup>Lu SPECT imaging of patients having treatment cycles of 7.4 GBq administered with concomitant infusion of an amino-acid solution for renal protection.

#### Uppsala

Uppsala reported dosimetry evaluations in a regimen in which subsequent treatment cycles were given until either the total absorbed dose to the kidneys reached 23 Gy or the bone marrow dose reached 2 Gy (19,60). Tumor-absorbed doses were also evaluated in a study by Ilan et al. (55). In the routine protocol absorbed doses to kidneys and other organs were determined from the SPECT/CT imaging performed during the first treatment at 24, 96, and 168 h after administration and 1 SPECT/CT study at 24 h in the following cycles. The SPECT/CT scans were obtained

using ME collimators and 120 projection angles with acquisition time equal to 30 s per frame. An energy window of 20% was centered on the 208-keV photopeak, and projection data were stored in  $128 \times 128$  matrices. SPECT reconstruction was performed using software available on the clinical workstation. An iterative OSEM algorithm with 4 iterations and 8 subsets and postfiltering using a Hann filter with a cutoff of 0.85 were used (19,60). AC based on a low-dose CT image was included in the reconstruction, but corrections for scatter and collimator response were not included. SPECT image calibration was implemented by imaging a 100-mL  $^{177}\text{Lu}$  sphere placed inside an elliptic water-filled cylinder. The counting rate in a spheric  $4 \text{ cm}^3$  VOI placed centrally in the sphere in the reconstructed image was determined, and the activity concentration in kidneys was quantified using this VOI. A monoexponential function was fitted to the 3 data points to determine the cumulated activity concentration. The absorbed dose was calculated by multiplying the time-integrated activity concentration by the dose concentration factor, derived from the unit density sphere model of  $^{177}\text{Lu}$  (61) and thus taking self-dose into account (20).

### Lund

In the Lund/Gothenburg ongoing clinical trial (EudraCT no. 2011-000240-16), treatment continued until the total delivered renal biologically effective dose reached 27 Gy, or 40 Gy, depending on additional risk factors (4). Dosimetry was performed during every treatment cycle and was based on a hybrid SPECT/planar method, chosen as a compromise between the quantitative accuracy of SPECT and the need to visualize the whole-body tumor burden during the course of treatment. The SPECT/CT scans were acquired at 24 h after injection (Fig. 7), using 60 projections, each 45 s, in a 360-rotation mode. Scans were acquired using a single energy window centered on the 208-keV photopeak, with a width of 15% or 20%, depending on the energy resolution of the SPECT/CT systems used. ME collimators were used, and projection data were stored in  $128 \times 128$  matrices. The whole-body anterior–posterior planar imaging was performed at 0, 24 or 48 h, 96 h, and 168 h after injection. The acquired images were exported for further processing using the in-house software LundAdose (62). The renal time–activity curves were determined from this series of planar images that were corrected for attenuation, scatter, and overlapping tissue activity (17,63). SPECT reconstruction was performed by an iterative OSEM algorithm with 8 iterations and 10 subsets. Corrections for attenuation, scatter, and collimator response were included in the reconstruction, with the low-dose CT image used to generate AMs and scatter kernels for the ESSE method (49) precalculated using Monte Carlo methods (29).

Camera calibration for both SPECT- and planar-based quantification was derived from a planar scan of a known activity placed in a Petri dish in air. From the quantified SPECT image, maps of the absorbed dose rate were calculated using a Monte Carlo–based method in which a CT-derived 3-dimensional map of the tissue density distribution was used as an input (64). VOIs encompassing the cortex and medulla of the left and right kidneys were manually segmented based on the CT images. The absorbed dose rates were determined as the median values of activity within these VOIs, which were compensated for partial-volume effects using a recovery factor of 0.85, as determined experimentally. These SPECT-derived absorbed-dose rates were used to renormalize the time–activity curves obtained from planar images, giving

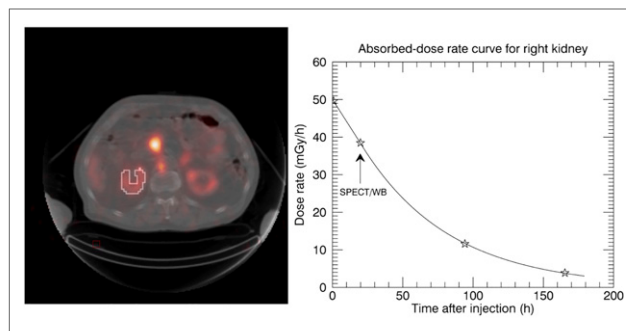


**FIGURE 7.** Reconstructed image (80 OSEM updates) from  $^{177}\text{Lu}$ -DOTATATE patient study measured at 24 h after injection with attenuation, scatter (ESSE), and collimator response compensation. ROI over right kidney is indicated. Small hot region is tumor. To right, time–activity curve shows calculated dose rate as function of time. Arrow indicates time where SPECT study was performed.

time-versus-dose rate curves from which values of the absorbed doses were calculated (65).

### CONCLUSION

There is a growing body of evidence that effectiveness of targeted radionuclide therapies could be greatly improved if they followed personalized plans based on patient-specific dosimetry calculations (16). Such calculations, however, require accurate information about the biodistribution of the radioactive therapeutic agent in the patient body, which must be obtained from quantitative imaging studies.

Although the medium-energy  $\beta^-$ -emissions of  $^{177}\text{Lu}$  make it useful for many radionuclide therapy applications, its  $\gamma$ -emissions are suitable for quantitative imaging necessary for dosimetry calculations. This document, which follows the general overview of quantitative imaging principles to be used in radionuclide therapy studies presented in the pamphlet by Dewaraja et al. (33), describes methods that are specifically recommended for use in  $^{177}\text{Lu}$  quantitative studies. A detailed discussion of the effects that can affect the quantitative accuracy of the estimated activity distribution and a series of recommendations and guidelines are provided. The discussed effects and recommendations are illustrated by example images and are supported by numeric data obtained from simulations, phantom experiments, and patient studies.

### DISCLOSURE

Support was granted by the Swedish Research Council, the Bertha Kamprad Foundation and the Gunnar Nilsson Cancer Foundation. No other potential conflict of interest relevant to this article was reported.

### REFERENCES

1. Kyker GC, Christopherson WM, Berg HF, Brucer M. Selective irradiation of lymph nodes by radiolutecium (Lu 177). *Cancer*. 1956;9:489–498.
2. Kwekkeboom DJ, de Herder W, Kam B, et al. Treatment with the radiolabeled somatostatin analog [ $^{177}\text{Lu}$ -DOTA 0,Tyr3]octreotate: toxicity, efficacy, and survival. *J Clin Oncol*. 2008;26:2124–2130.
3. Imhof A, Brunner P, Marincek N, et al. Response, survival, and long-term toxicity after therapy with the radiolabeled somatostatin analogue [ $^{90}\text{Y}$ -DOTA]-TOC in metastasized neuroendocrine cancers. *J Clin Oncol*. 2011;29:2416–2423.

4. Bodei L, Cremonesi M, Ferrari M, et al. Long-term evaluation of renal toxicity after peptide receptor radionuclide therapy with <sup>90</sup>Y-DOTATOC and <sup>177</sup>Lu-DOTATATE: the role of associated risk factors. *Eur J Nucl Med Mol Imaging*. 2008;35:1847–1856.
5. Kam BL, Teunissen JJ, Krenning EP, et al. Lutetium-labelled peptides for therapy of neuroendocrine tumours. *Eur J Nucl Med Mol Imaging*. 2012;39: S103–S112.
6. Bodei L, Kidd M, Paganelli G, et al. Long-term tolerability of PRRT in 807 patients with neuroendocrine tumours: the value and limitations of clinical factors. *Eur J Nucl Med Mol Imaging*. 2015;42:5–19.
7. Forrer F, Oechslein-Oberholzer C, Campana B, et al. Radioimmunotherapy with <sup>177</sup>Lu-DOTA-rituximab: final results of a phase I/II study in 31 patients with relapsing follicular, mantle cell, and other indolent B-cell lymphomas. *J Nucl Med*. 2013;54:1045–1052.
8. Stillebroer AB, Zegers CM, Boerman OC, et al. Dosimetric analysis of <sup>177</sup>Lu-cG250 radioimmunotherapy in renal cell carcinoma patients: correlation with myelotoxicity and pretherapeutic absorbed dose predictions based on <sup>111</sup>In-cG250 imaging. *J Nucl Med*. 2012;53:82–89.
9. Vallabhajosula S, Goldsmith SJ, Hamacher KA, et al. Prediction of myelotoxicity based on bone marrow radiation-absorbed dose: radioimmunotherapy studies using <sup>90</sup>Y- and <sup>177</sup>Lu-labeled J591 antibodies specific for prostate-specific membrane antigen. *J Nucl Med*. 2005;46:850–858.
10. Meredith R, You Z, Alvarez R, Partridge E, Grizzle W, LoBuglio A. Predictors of long-term outcome from intraperitoneal radioimmunotherapy for ovarian cancer. *Cancer Biother Radiopharm*. 2012;27:36–40.
11. David KA, Milowsky MI, Kostakoglu L, et al. Clinical utility of radiolabeled monoclonal antibodies in prostate cancer. *Clin Genitourin Cancer*. 2006;4:249–256.
12. Bander NH, Milowsky MI, Nanus DM, Kostakoglu L, Vallabhajosula S, Goldsmith SJ. Phase I trial of <sup>177</sup>lutetium-labeled J591, a monoclonal antibody to prostate-specific membrane antigen, in patients with androgen-independent prostate cancer. *J Clin Oncol*. 2005;23:4591–4601.
13. Tagawa ST, Milowsky MI, Morris M, et al. Phase II study of lutetium-<sup>177</sup>-labeled anti-prostate-specific membrane antigen monoclonal antibody J591 for metastatic castration-resistant prostate cancer. *Clin Cancer Res*. 2013;19:5182–5191.
14. Schoffelen R, Boerman OC, Goldenberg DM, et al. Development of an imaging-guided CEA-pretargeted radionuclide treatment of advanced colorectal cancer: first clinical results. *Br J Cancer*. 2013;109:934–942.
15. Schoffelen R, Woliner-van der Weg W, Visser EP, et al. Predictive patient-specific dosimetry and individualized dosing of pretargeted radioimmunotherapy in patients with advanced colorectal cancer. *Eur J Nucl Med Mol Imaging*. 2014;41: 1593–1602.
16. Strigari L, Konijnenberg M, Chiesa C, et al. The evidence base for the use of internal dosimetry in the clinical practice of molecular radiotherapy. *Eur J Nucl Med Mol Imaging*. 2014;41:1976–1988.
17. Garkavij M, Nickel M, Sjögreen-Gleisner K, et al. <sup>177</sup>Lu-[DOTA<sub>0</sub>Tyr<sub>3</sub>] octreotate therapy in patients with disseminated neuroendocrine tumors: analysis of dosimetry with impact on future therapeutic strategy. *Cancer*. 2010;116:1084–1092.
18. Guerriero F, Ferrari ME, Botta F, et al. Kidney dosimetry in <sup>177</sup>Lu and <sup>90</sup>Y peptide receptor radionuclide therapy: influence of image timing, time-activity integration method, and risk factors. *Biomed Res Int*. 2013;2013: 935351.
19. Sandström M, Garske-Roman U, Granberg D, et al. Individualized dosimetry of kidney and bone marrow in patients undergoing <sup>177</sup>Lu-DOTA-octreotate treatment. *J Nucl Med*. 2013;54:33–41.
20. Sandström M, Garske U, Granberg D, Sundin A, Lundqvist H. Individualized dosimetry in patients undergoing therapy with <sup>177</sup>Lu-DOTA-D-Phe (1)-Tyr (3)-octreotate. *Eur J Nucl Med Mol Imaging*. 2010;37:212–225.
21. Cremonesi M, Ferrari M, Di Dia A, et al. Recent issues on dosimetry and radiobiology for peptide receptor radionuclide therapy. *Q J Nucl Med Mol Imaging*. 2011;55:155–167.
22. Kondev FG. Nuclear data sheets for A = 177. *Nucl Data Sheets (NY NY)*. 2003;98:801–1095.
23. Deepa S, Vijay Sai K, Gowrishankar R, Rao D, Venkataramiah K. Precision electron-gamma spectroscopic measurements in the decay of <sup>177</sup>Lu. *Appl Radiat Isot*. 2011;69:869–874.
24. Schötzig U, Schrader H, Schonfeld E, Gunther E, Klein R. Standardisation and decay data of <sup>177</sup>Lu and <sup>188</sup>Re. *Appl Radiat Isot*. 2001;55:89–96.
25. Kossert K, Nahle OJ, Ott O, Dersch R. Activity determination and nuclear decay data of <sup>177</sup>Lu. *Appl Radiat Isot*. 2012;70:2215–2221.
26. Eckerman KF, Endo A. *MIRD: Radionuclide Data and Decay Schemes*. 2nd ed. Reston, VA: Society of Nuclear Medicine; 2008.
27. Kondev FG. Table of radionuclides. In: Be MM, Criste V, Dulieu C, et al., eds. Vol 2. Sèvres, France: Bureau International des Poids et Mesures; 2004:107–112.
28. NuDat2.6. National Nuclear Data Center website. <http://www.nndc.bnl.gov/nudat2/>. Accessed November 4, 2015.
29. Ljungberg M, Strand SE. A Monte Carlo program for the simulation of scintillation camera characteristics. *Comput Methods Programs Biomed*. 1989;29:257–272.
30. Shcherbinin S, Piwowska-Bilska H, Celler A, Birkenfeld B. Quantitative SPECT/CT reconstruction for <sup>177</sup>-Lu and <sup>177</sup>-Lu/<sup>90</sup>-Y targeted radionuclide therapies. *Phys Med Biol*. 2012;57:5733–5747.
31. Segars WP, Sturgeon G, Mendonca S, Grimes J, Tsui BMW. 4D XCAT phantom for multimodality imaging research. *Med Phys*. 2010;37:4902–4915.
32. Brodin G, Gustafsson J, Ljungberg M, Sjögreen Gleisner K. Digital reference phantoms for accuracy assessment of image-based dosimetry in <sup>177</sup>Lu peptide receptor radionuclide therapy. Paper presented at: 5th International Symposium on Targeted Radionuclide-therapy and Dosimetry (ISTARD), European Association of Nuclear Medicine Annual Meeting; October, 18–22, 2014; Gothenburg, Sweden.
33. Dewaraja YK, Frey EC, Sgouros G, et al. MIRD pamphlet no. 23: quantitative SPECT for patient-specific 3-dimensional dosimetry in internal radionuclide therapy. *J Nucl Med*. 2012;53:1310–1325.
34. Lyra M, Ploussi A. Filtering in SPECT image reconstruction. *Int J Biomed Imaging*. 2011;2011:693795.
35. Cheng L, Hobbs RF, Segars PW, Sgouros G, Frey EC. Improved dose-volume histogram estimates for radiopharmaceutical therapy by optimizing quantitative SPECT reconstruction parameters. *Phys Med Biol*. 2013;58:3631–3647.
36. Cherry SR, Sorensen JA, Phelps ME. *Physics in Nuclear Medicine*. 3rd ed. Philadelphia, PA: Saunders; 2003.
37. Strand SE, Lamm IL. Theoretical studies of image artifacts and counting losses for different photon fluence rates and pulse-height distributions in single-crystal NaI(Tl) scintillation cameras. *J Nucl Med*. 1980;21:264–275.
38. Delpont G, Ferrer L, Lisboa A, Bardies M. Correction of count losses due to deadtime on a DST-XLi (SmVi-GE) camera during dosimetric studies in patients injected with iodine-131. *Phys Med Biol*. 2002;47:N79–90.
39. Celler A, Piwowska-Bilska H, Shcherbinin S, Uribe C, Mikolajczak R, Birkenfeld B. Evaluation of dead-time corrections for post-radionuclide-therapy <sup>177</sup>Lu quantitative imaging with low-energy high-resolution collimators. *Nucl Med Commun*. 2014;35:73–87.
40. Koral KF, Zasadny KR, Ackermann RJ, Ficaro EP. Deadtime correction for two multihead Anger cameras in <sup>131</sup>I dual-energy-window-acquisition mode. *Med Phys*. 1998;25:85–91.
41. Shepp LA, Vardi Y. Maximum likelihood reconstruction for emission tomography. *IEEE Trans Med Imaging*. 1982;1:113–122.
42. Hudson HM, Larkin RS. Accelerated image reconstruction using ordered subsets of projection data. *IEEE Trans Med Imaging*. 1994;13:601–609.
43. Goetze S, Wahl RL. Prevalence of misregistration between SPECT and CT for attenuation-corrected myocardial perfusion SPECT. *J Nucl Cardiol*. 2007;14:200–206.
44. Ogawa K, Harata Y, Ichihara T, Kubo A, Hashimoto S. A practical method for position-dependent Compton-scatter correction in single photon emission CT. *IEEE Trans Med Imaging*. 1991;10:408–412.
45. de Nijs R, Lagerburg V, Klausen TL, Holm S. Improving quantitative dosimetry in <sup>177</sup>Lu-DOTATATE SPECT by energy window-based scatter corrections. *Nucl Med Commun*. 2014;35:522–533.
46. Beauregard JM, Hofman MS, Pereira JM, Eu P, Hicks RJ. Quantitative <sup>177</sup>Lu SPECT (QSPECT) imaging using a commercially available SPECT/CT system. *Cancer Imaging*. 2011;11:56–66.
47. Zeintl J, Vija AH, Yahil A, Hornegger J, Kuwert T. Quantitative accuracy of clinical <sup>99m</sup>Tc SPECT/CT using ordered-subset expectation maximization with 3-dimensional resolution recovery, attenuation, and scatter correction. *J Nucl Med*. 2010;51:921–928.
48. Hutton BF, Buvat I, Beekman FJ. Review and current status of SPECT scatter correction. *Phys Med Biol*. 2011;56:R85–R112.
49. Frey EC, Tsui BMW. A new method for modeling the spatially-variant, object-dependent scatter response function in SPECT. *IEEE Nucl Sci Symp*. 1996;2:1082–1086.
50. Frey EC, Ju ZW, Tsui BMW. A fast projector-backprojector pair modeling the asymmetric, spatially varying scatter response function for scatter compensation in SPECT imaging. *IEEE Trans Nucl Sci*. 1993;40:1192–1197.
51. Vandervoort E, Celler A, Harrop R. Implementation of an iterative scatter correction, the influence of attenuation map quality and their effect on absolute quantitation in SPECT. *Phys Med Biol*. 2007;52:1527–1545.

52. Wells RG, Celler A, Harrop R. Analytical calculation of photon distributions in SPECT projections. *IEEE Trans Med Imaging*. 1998;45:3202–3214.
53. Erlandsson K, Buvat I, Pretorius PH, Thomas BA, Hutton BF. A review of partial volume correction techniques for emission tomography and their applications in neurology, cardiology and oncology. *Phys Med Biol*. 2012;57:R119–R159.
54. Uribe C, Celler A, Beauregard JM. Planar vs. tomographic determination of normalization factors for absolute quantitation of SPECT/CT studies. *Eur J Nucl Med Mol Imaging*. 2014;41:331.
55. Ilan E, Sandstrom M, Wassberg C, et al. Dose response of pancreatic neuroendocrine tumors treated with peptide receptor radionuclide therapy using <sup>177</sup>Lu-DOTATATE. *J Nucl Med*. 2015;56:177–182.
56. Uribe C, Celler A, Frauenstein L, et al. Accuracy of Lu-177 quantitation for dosimetry in patients undergoing neuro-endocrine tumors radionuclide therapy. *Eur J Nucl Med Mol Imaging*. 2014;41:S332.
57. Vennart J. Limits for intakes of radionuclides by workers: ICRP publication 30. *Health Phys*. 1981;40:477–484.
58. Valkema R, Pauwels SA, Kvols LK, et al. Long-term follow-up of renal function after peptide receptor radiation therapy with <sup>90</sup>Y-DOTA(0),Tyr(3)-octreotide and <sup>177</sup>Lu-DOTA(0), Tyr(3)-octreotate. *J Nucl Med*. 2005;46(suppl 1):83S–91S.
59. Swärd C, Bernhardt P, Ahlman H, et al. [<sup>177</sup>Lu-DOTA 0-Tyr 3]-octreotate treatment in patients with disseminated gastroenteropancreatic neuroendocrine tumors: the value of measuring absorbed dose to the kidney. *World J Surg*. 2010;34:1368–1372.
60. Garske U, Sandstrom M, Johansson S, et al. Minor changes in effective half-life during fractionated <sup>177</sup>Lu-octreotate therapy. *Acta Oncol*. 2012;51:86–96.
61. Stabin MG, Sparks RB, Crowe E. OLINDA/EXM: the second-generation personal computer software for internal dose assessment in nuclear medicine. *J Nucl Med*. 2005;46:1023–1027.
62. Sjögreen K, Ljungberg M, Wingardh K, Minarik D, Strand SE. The LundADose method for planar image activity quantification and absorbed-dose assessment in radionuclide therapy. *Cancer Biother Radiopharm*. 2005;20:92–97.
63. Gleisner KS, Ljungberg M. Patient-specific whole-body attenuation correction maps from a CT system for conjugate-view-based activity quantification: method development and evaluation. *Cancer Biother Radiopharm*. 2012;27:652–664.
64. Sjögreen-Gleisner K, Rueckert D, Ljungberg M. Registration of serial SPECT/CT images for three-dimensional dosimetry in radionuclide therapy. *Phys Med Biol*. 2009;54:6181–6200.
65. Gustafsson J, Nilsson P, Gleisner KS. On the biologically effective dose (BED)-using convolution for calculating the effects of repair: II. Numerical considerations. *Phys Med Biol*. 2013;58:1529–1548.
66. Grimes J, Celler A, Shcherbinin S, Piwowarska-Bilska H, Birkenfeld B. The accuracy and reproducibility of SPECT target volumes and activities estimated using an iterative adaptive thresholding technique. *Nucl Med Commun*. 2012;33:1254–1266.